94 GHz Radar Backscatter Characteristics of Alpine Glacier Ice

W. D. Harcourt[1,2] , D. A. Robertson[1], D. G. Macfarlane[1], B. R. Rea[2], and M. Spagnolo[2]

[1]SUPA School of Physics and Astronomy, University of St Andrews, St Andrews, UK, [2]School of Geosciences, University of Aberdeen, Aberdeen, UK

Abstract Measuring the radar backscatter characteristics of glacier ice at different frequencies and incidence angles is fundamental to predicting the glacier mapping performance of a sensor. However, such measurements at 94 GHz do not exist. To address this knowledge gap, we collected 94 GHz radar backscatter data from the surface of Rhônegletscher in Switzerland using the All-Weather Volcano Topography Imaging Sensor (AVTIS2) real-aperture Frequency Modulated Continuous Wave radar. We determine the mean normalized radar cross section (σ^0_{mean}) to be −9.9 dB. The distribution closely follows a log-normal distribution with a high goodness of fit ($R^2 = 0.99$) which suggests that radar backscatter is diffuse and driven by surface roughness. Further, we quantified the uncertainty of AVTIS2 3D point clouds to be 1.30–3.72 m, which is smaller than other ground-based glacier surface mapping radars. These results demonstrate that glacier surfaces are an efficient scattering target at 94 GHz, hence demonstrating the suitability of millimeter-wave radar for glacier monitoring.

Plain Language Summary Radar sensors map glacier surfaces by transmitting a signal at a specific frequency and measuring its return strength when reflected back. This returned signal strength, called radar backscatter, is determined by the characteristics of the glacier surface and varies with radar frequency and sensor viewing angle. Millimeter-wave radars operating at 94 GHz can acquire high resolution measurements of glaciers in most weather conditions. However, there are currently no measurements of radar backscatter from glacier surfaces at this frequency. We therefore acquired the first ever measurements of 94 GHz radar backscatter from glacier ice. The results are consistent with those expected from randomly rough surfaces, hence we conclude that the roughness of the glacier surface is the primary driver of 94 GHz radar backscatter. We also show that 3D glacier surface mapping at this frequency is more accurate than other ground-based radars that are employed to map glacier geometries. The results overall indicate that 94 GHz radar is an effective tool for glacier monitoring and thus opens up new possibilities for studying glacier processes.

1. Introduction

High frequency radar, such as those operating at W-band (75–110 GHz), offer the ability to achieve high spatial resolution mapping of glacier surfaces in most weather conditions using a practical field portable system. Additionally, they are highly sensitive to changes in surface conditions due to their shorter wavelength and hence have the potential to detect changes over time (Harcourt, Robertson, Macfarlane, Rea, Spagnolo, Benn, & James, 2023). For example, millimeter-scale roughness, which is at the same scale as 94 GHz radar (3.19 mm), is a function of the ice crystals which form the glacier, diurnal to seasonal melting and refreezing on the glacier surface, the transport and deposition of fine-grained sediment (e.g., windblown dust) and organic material such as cryoconite, and local roughness variations. Further, glacier structures, such as foliation, folds, and faults (Benn & Evans, 2010; Hambrey & Lawson, 2000; Hudleston, 2015; Jennings & Hambrey, 2021) become exposed at the glacier surface in the ablation zone as a result of ice flow and surface melt. Surface melt may also form supraglacial streams which range in size from centimeters to tens of meters. Therefore, quantifying the radar backscatter characteristics of glacier surfaces is important for: (a) predicting the glacier mapping performance of a radar system and (b) evaluating how this information can be used to understand highly dynamic glaciological processes such as iceberg calving, diurnal surface melting, glacial lake outburst floods.

Radar backscatter from natural surfaces varies with operating frequency and the incidence angle of the radar beam to the surface (Rees, 1992; F. Ulaby et al., 2019). W-band radar backscatter measurements from glacier surfaces are scarce and there are no measurements reported at 94 GHz. Foessel et al. (1999) showed that short-range (<50 m) 77 GHz radar backscatter from blue ice terrain in Antarctica is driven by surface roughness features such as ice cups that form through localized melting and sublimation. In comparison, W-band radar backscatter

Software: W. D. Harcourt, D. A. Robertson, D. G. Macfarlane
Supervision: D. A. Robertson, D. G. Macfarlane, B. R. Rea, M. Spagnolo
Visualization: W. D. Harcourt
Writing – original draft: W. D. Harcourt
Writing – review & editing: W. D. Harcourt, D. A. Robertson, D. G. Macfarlane, B. R. Rea, M. Spagnolo

from snow surfaces have been widely reported (N. C. Currie et al., 1992; F. T. Ulaby et al., 1998; F. Ulaby et al., 2019). W-band radar backscatter from snow reduces exponentially with increasing liquid water content (Williams et al., 1988; N. Currie et al., 1988) and increases as the snow surface becomes more rough (F. T. Ulaby et al., 1998). A refrozen snowpack, which most closely resembles a glacier surface, contains larger snow grains than both wet and dry snowpacks which reduces the capacity of the snowpack to retain moisture (Chang et al., 1996) and thus increases radar backscatter (N. C. Currie et al., 1992). Therefore, both dry and refrozen snow may contain a volume scattering component which depends on snow density (Kuga et al., 1991; Williams et al., 1988) but the presence of liquid moisture inhibits signal penetration and thus surface scattering dominates from wet snow.

In light of the preceding discussion, this study has three key aims:

1. Quantify the relationship between incidence angle and radar backscatter for alpine glacier ice at 94 GHz.
2. Determine drivers of 94 GHz radar backscatter from alpine glacier surfaces.
3. Assess the accuracy of 94 GHz radar measurements of glacier topography.

2. Materials and Methods

2.1. Data Collection

Radar backscatter data were collected from the terminal portion of Rhônegletscher in Switzerland (Figure 1) on 3 and 4 September 2019 using the second generation All-Weather Volcano Topography Imaging Sensor (AVTIS2) 94 GHz Frequency Modulated Continuous Wave radar (Harcourt, Macfarlane, & Robertson, 2023; Macfarlane et al., 2013). AVTIS2 transmits a circular beam pattern with a two-way beamwidth of 0.35° and VV polarisation. Rhônegletscher is a polythermal, alpine glacier that terminates in an ice-contact lake and whose south-eastern terminus is partially covered by tarpaulin to locally reduce surface ablation. Two lateral moraines consisting of unconsolidated sediment are present on both sides of the glacier, whilst polished bedrock is exposed on the western margin (Figure 1). AVTIS2 was positioned ~250 m from the glacier terminus at an elevation of 2,314 m a.s.l (Figure 1) and deployed on both days with a range resolution of 0.75 m and a maximum range of ~6 km. Meteorological data was acquired from the Grimsel Hospiz Weather Station (1,980 m a.s.l) located on the western side of Gärstenhörner and ~3 km west of the Rhônegletscher snout (Figure 1). The average air temperature was 10.1°C on day 1 and 12.4°C day 2, with clear skies throughout, whilst average water vapor density was 6.7 g/m^3 on day 1 and 7.3 g/m^3 on day 2.

2.2. 3D Point Cloud Accuracy Assessment

AVTIS2 mechanically scans across a target landscape and produces a 3D data cube of radar backscatter at each range bin, azimuth angle and elevation angle (R, θ, ϕ). Radar data acquisition lasted ~2.5 hr on 3 September and ~5.75 hr on 4 September. 3D point clouds were extracted from the data cubes measured on both days following the methodology described by Harcourt, Macfarlane, and Robertson (2023): (a) average neighboring Line of Sight (LoS) waveforms, (b) convert to Signal-to-Noise Ratio (SNR), (c) extract the maximum SNR along each LoS (single-point) or the range to all SNR targets larger than 2X the standard deviation of the SNR range profile (multiple-point), and (d) remove low SNR points and spatially isolated point cloud outliers. The resulting 3D point clouds are georeferenced to an Earth-Centered Earth-Fixed (ECEF) cartesian coordinate system using the (x, y, z) dGPS position of Ground Control Points (GCPs) measured on 4 September (see Figure 1 for locations). GCPs were deployed on the glacier surface and not on the surrounding bedrock to ensure dominant scattering targets such as boulders did not obstruct the returned signal from the trihedral reflector. This resulted in a poor angular spread of the GCPs with a small bias toward the western margin of the glacier (Figure 1). The value of z for each GCP is measured relative to the WGS84 Earth surface ellipsoid model, hence it was converted to height above sea level (a.s.l) by differencing the EGM96 Geopotential Model geoid from point cloud heights. The average correction was ~50 m.

The accuracy of the AVTIS2 3D point clouds was quantified through a comparison with a 50 cm Digital Elevation Model (DEM) extracted from aerial photogrammetry acquired ~1 week before this field study (© swisstopo). This DEM does not contain a published error estimate, although photogrammetry errors are usually on the order of a few millimeters (James et al., 2017). The comparison was computed using the
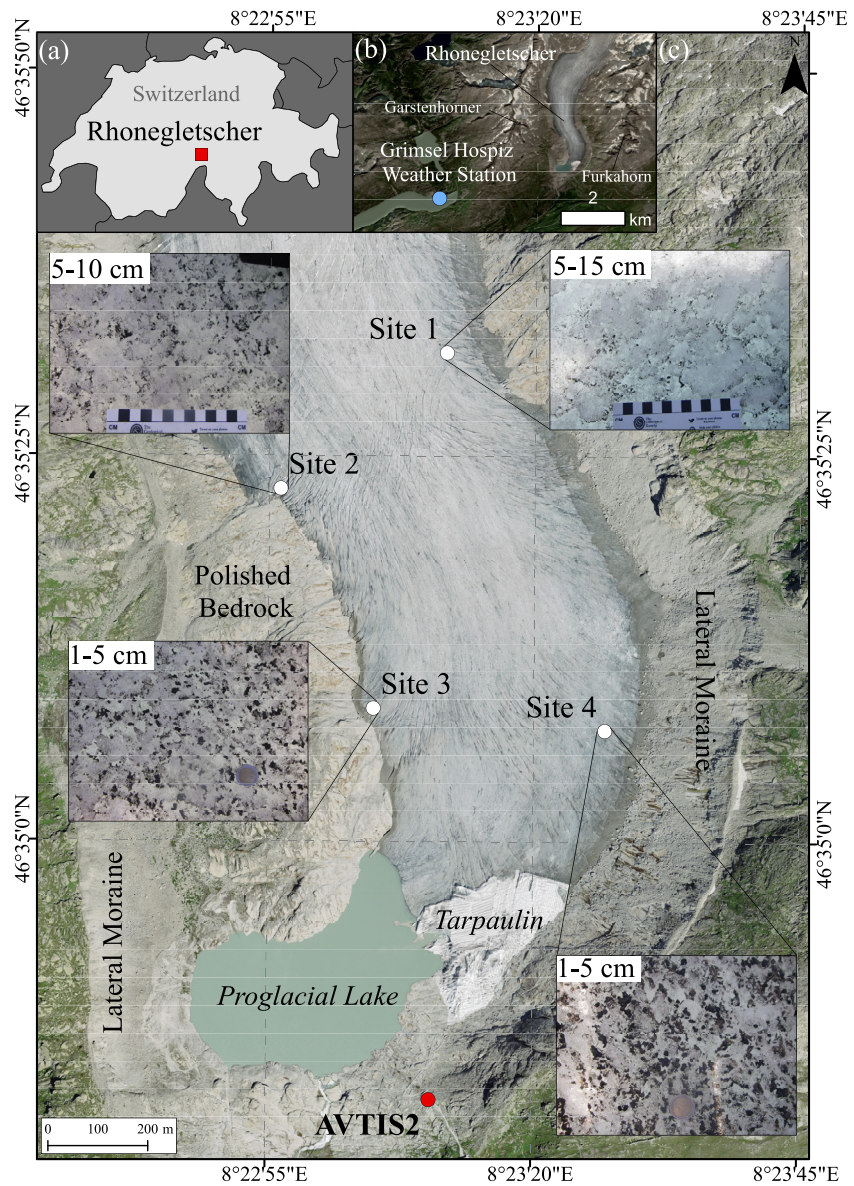
Figure 1. The location of (a) Rhônegletscher and (b) the Grimsel Hospiz weather station. (c) Annotated aerial photo of Rhônegletscher. At each site, a trihedral corner reflector was positioned for georeferencing and range autofocusing, whilst notes and pictures of ice properties were also recorded (notice coins or rulers for scale). Aerial imagery was acquired in 2020 from © swisstopo.

Cloud-to-Mesh (C2M) technique which compares the height difference between each point in the AVTIS2 point cloud with the height of a pixel in the DEM (Girardeau-Montaut et al., 2005; Lague et al., 2013). The positional uncertainty of the AVTIS2 point cloud is then estimated as the standard deviation (σ_{A2}) of these distance measurements:

$$\sigma_{A2} = \sqrt{\frac{1}{N}\sum_{i=1}^{N}\left(l_i - \bar{l}\right)^2} \qquad (1)$$

where l_i is an individual C2M measurement, $\bar{l}$ is the mean of l_{A2}, and N is the total number of points in the point cloud. The value of $\bar{l}$ indicates the existence of systematic errors associated with the AVTIS2 measurements, whilst σ_{A2} is a measure of point cloud precision.
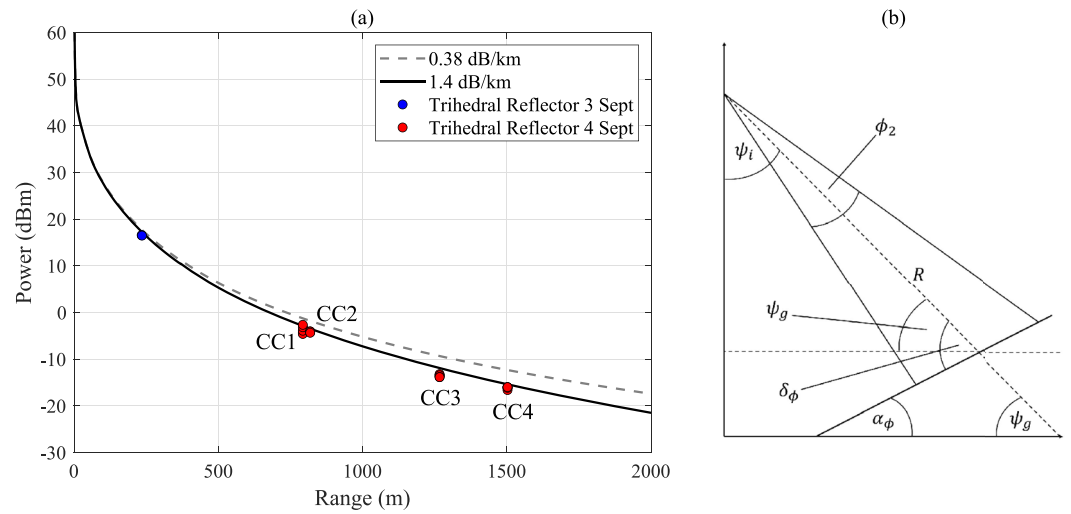
Figure 2. (a) Predicted radar received power (P_r) as a function of range for a 20 dBsm trihedral radar reflector. The dashed line represents P_r with atmospheric attenuation predicted directly from the ITU model (ITU-R, 2013, ITU-R676-10) using measurements of air temperature (12.4°C), atmospheric pressure (80,788 Pa), and water vapor density (7.3 g/m³) on day 2. The solid black line represents P_r with the 1.4 dB/km atmospheric attenuation to account for an increase water vapor density over the glacier surface. (b) Radar geometry, variables described in text.

2.3. Radar Calibration

AVTIS2 radar received power (P_r) was calibrated by measuring P_r of four trihedral corner reflectors with a radar cross section (σ) of 20 dBsm at multiple distances from the radar and comparing it to the received power predicted by the radar range equation (Nathanson et al., 1999):

$$P_r = \frac{P_t G_{\text{ant}}^2 G_{\text{rec}} \lambda^2 \sigma}{(4\pi)^3 R^4 (2L_\alpha) L_h} \tag{2}$$

here, P_t is transmit power (16.4 dBm), G_{ant} is antenna gain (51.4 dBi), G_{rec} is the Intermediate Frequency (IF) gain (see Supporting Information S1), λ is the radar wavelength (3.19 mm), R is range, and L_h represents losses within the radar receiver chain (~8.7 dB). The two-way atmospheric attenuation parameter ($2L_\alpha$) was estimated from the International Telecommunication Union (ITU) Signal Attenuation Model for atmospheric gases (ITU-R, 2013, ITU-R676-10) using the daily average meteorological data from Grimsel Hospiz as input (Figure 2). These values of L_α (0.35 dB/km on day 1, 0.38 dB/km on day 2) are unrealistic for radar signals propagating across a glacier surface where water vapor density is expected to be higher as a result of locally enhanced surface melting (van den Broeke, 1997). Therefore, a higher attenuation factor of 1.4 dB/km is used on both days, which better fits the received power from a 20 dBsm trihedral reflector at different ranges (Figure 2).

The Normalized Radar Cross Section (σ^0) is the quantity of interest for distributed terrain clutter such as glacier surfaces and is given by:

$$\sigma^0 = P_r \cdot \frac{(4\pi)^3 R^3 (2L_\alpha) L_c}{P_t G_{\text{ant}}^2 G_{\text{rec}} \lambda^2} \cdot \frac{\cos\delta_\phi}{\theta_2 \Delta R} \tag{3}$$

here, ΔR is the size of the range bin (0.75 m), P_r is the locally averaged radar received power from the single-point methodology (Harcourt, Macfarlane, & Robertson, 2023), θ_2 is the two-way radar beamwidth in azimuth (0.33°), and δ_ϕ is the local incidence angle in elevation (Figure 2b). Both θ_2 and δ_ϕ are in radians. For each terrain point, a set of neighboring points ($c_{\text{nn}}(\theta, \phi)$) was extracted within an angular radius of 0.26° (i.e., half the AVTIS2 one-way beamwidth) and limited in range by ±10 m. The local surface slope in the elevation direction (δ_ϕ) was then estimated using the following:

$$\delta_\phi = \psi_g + \arctan\left(\frac{z}{R}\right) \tag{4}$$

here, z/R (α_ϕ in Figure 2b) represents the surface slope of c_{nn}, whilst ψ_g is the radar grazing angle and is equal to the elevation angle (ϕ) associated with each point in the point cloud. Values of σ^0 are reported in terms of incidence angle (ψ_i):

$$\psi_i = 90 - \delta_\phi \qquad (5)$$

which follows previous convention (F. Ulaby et al., 2019). Glacier and non-glacier terrain were extracted using the 2019 Rhônegletscher outlines from the Global Land and Ice Measurements from Space (GLIMS) (Paul et al., 2015), which was edited to remove non-glacier features such as the tarpaulin cover.

3. Results and Discussion

3.1. 3D Glacier Topography

Figure 3a shows the photogrammetry DEM (© swisstopo) and Figure 3b shows, to the authors' knowledge, the first ever 3D point cloud of a glacier acquired using millimeter-wave radar at 94 GHz. Data from both days were combined to form a point cloud containing 283,742 points (single-point) and 563,601 points (multiple-point), respectively. The point cloud density is range dependent and varied from 16.4 points per m² at the glacier snout to 1.15 points per km² across the mountain peaks. Averaging the glacier and non-glacier uncertainties (σ_{A2}) (See Supporting Information S1) shows that σ_{A2} over glacier ice was ±2.75 m and over non-glacier terrain was ±3.66 m, which is a difference of 0.91 m (33%). The lower point cloud uncertainty over the glacier surface may in part be due to the more gradual surface slope of Rhônegletscher compared to the more irregular topography of the surrounding bedrock and moraine deposits (Figure 3a). The mean error $\left(\bar{l}\right)$ over glacier terrain was −1.03 m which is larger than the radar range resolution (0.75 m) but smaller than the uncertainty of both the single-point (±1.30 m) and multiple-point (±3.19 m) point clouds. Annual ice elevation change at Rhônegletscher was up to 20 m yr⁻¹ (Huss et al., 2021) which corresponds to up to 0.4 m over the 1 week between the photogrammetry and AVTIS2 data acquisitions. Therefore, the larger error may be due to a combination of both surface drawdown due to melting and an under-estimation of glacier surface elevation resulting from a poor angular spread of GCPs across the glacier.

The results presented here demonstrate that millimeter-wave radar point clouds acquired over alpine glacier surfaces are of sufficient quality for glaciological studies. The quoted uncertainty values are lower than those published for other close-range radar sensors which have been previously used in glaciological studies. The uncertainty of DEMs extracted from interferometric measurements using the GAMMA Portable Radar Interferometer have been estimated to be ~5 m below 9 km range over stable terrain in Greenland (Wang et al., 2022). Similarly, errors from DEM extraction using GB-SAR interferometric measurements across Belvedere Glacier in the Italian Alps were estimated to be >10 m (Noferini et al., 2009). Using radar interferometry to extract glacier topography yields larger errors and uncertainties compared to AVTIS2 due to the sensitivity of phase-based measurements to atmospheric variability, which is in agreement with previous studies (Harcourt, Macfarlane, & Robertson, 2023). Therefore, using real-beam millimeter-wave radar to map the 3D shape of glacier surfaces leads to more accurate results compared to both lower frequency radars and those using interferometry, and can be used to achieve higher angular resolution. This provides justification for using millimeter-wave radar in glaciological studies.

3.2. σ^0 of Glacier Terrain at 94 GHz

The σ^0 distribution for glacier terrain extracted from data collected on 4 September is shown in Figure 4a. The mean value of σ^0 $\left(\sigma^0_{mean}\right)$ is −9.9 dB. The minimum and maximum values of the distribution are taken to be the 5th $\left(\sigma^0_{5\%}\right)$ and 95th $\left(\sigma^0_{95\%}\right)$ percentiles and are calculated for glacier terrain as −17.0 and −3.4 dB, respectively (Figure 4a). Using the region between the 5th and 95th percentiles as the distribution limits, σ^0 for alpine glacier terrain at 94 GHz can be stated as: $-17.0 < \sigma^0 < -3.4$; $\sigma^0_{mean} = -9.9$ dB. The angular response of σ^0 between incidence angles 50° and 90°, which were the only observable angles in the field of view, is shown in Figure 4b, where the error bars represent the 5th and 95th percentiles. Using the mean values of σ^0 between 50° and 90° at 10° increments as shown in Figure 4b, σ^0 for alpine glacier terrain at 94 GHz is given as $-17.2 < \sigma^0 < 4.4$; $\sigma^0_{mean} = -7.0$ dB for $50° < \psi_i < 90°$ (N.B. the large negative error at 65° is ignored). Because the mean values at 55° and 65°
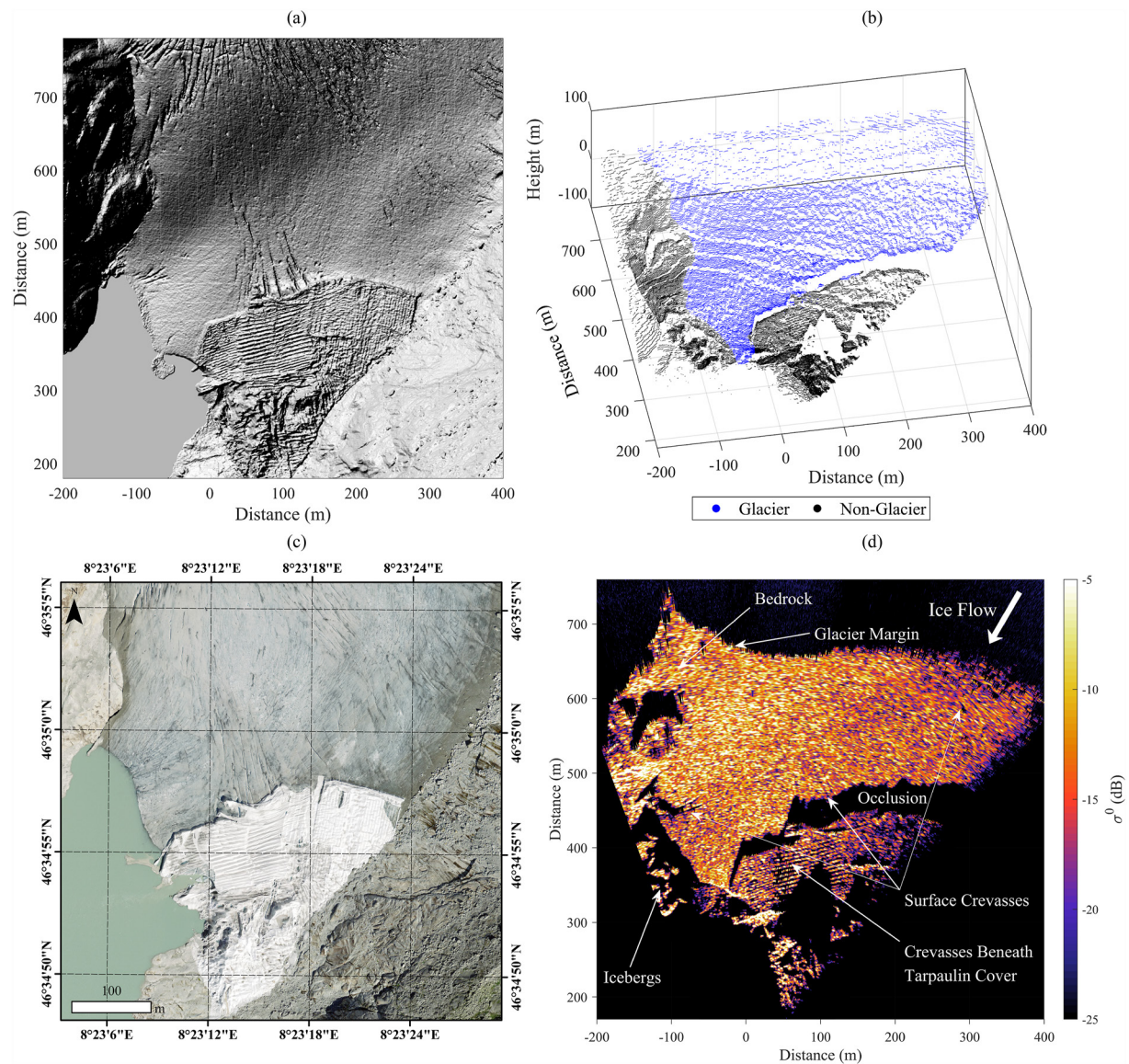
Figure 3. (a) Hillshade of the Rhônegletscher surface derived from an aerial photogrammetry DEM. Source: FOEN/swisstopo, provided by the VAR Glaciology Group and Glacier Monitoring in Switzerland groups. (b) AVTIS2 94 GHz point cloud over Rhônegletscher using the multiple-point methodology (563,601 points). The glacier (blue) was differentiated from non-glacier terrain (black) using the GLIMS glacier outlines (Paul et al., 2015). (c) Aerial image of the Rhônegletscher snout. (d) 2D 94 GHz σ^0 map of the Rhônegletscher snout with key features of the surface annotated. Note that because the AVTIS2 image is not georeferenced the alignment between panels (c) and (d) is not perfect.

contain a smaller number of samples, the range and mean of σ^0 using the distribution in Figure 4a is considered more accurate.

The σ^0 distribution in Figure 4a fits a Gaussian Probability Distribution Function (PDF) in dB (i.e., a Log-Normal distribution) with a high goodness of fit ($R^2 = 0.99$). This is considered reasonable given that the shorter wavelength of 94 GHz radar (3.19 mm) leads to a mostly random diffuse scattering pattern (N. C. Currie et al., 1992; F. Ulaby et al., 2019) and is primarily driven by surface roughness. Textural variations on the ice surface, driven by crevasses, debris cover, and supraglacial hydrology, further enhances the log-normal relationship. The consistency of σ^0 over high and medium incidence angles (50°–90°), which represents the "shadow" region where the radar beam is close to parallel with the ice surface, is also characteristic of terrain with a high surface roughness (F. Ulaby et al., 2019). Using measurements of ice crystal sizes (Figure 1) as an approximation for surface roughness (s), the wavelength-dependent roughness can be calculated using $2\pi s/\lambda$, where λ is the radar wavelength. Ice
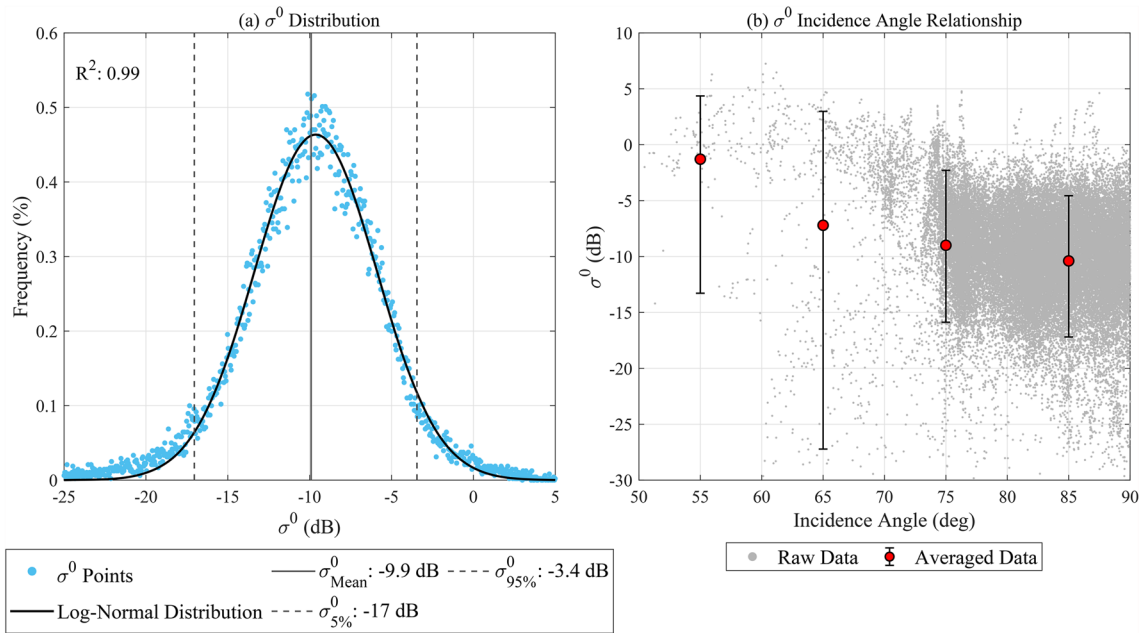
Figure 4. (a) The distribution of σ^0 values (blue dots) for glacier terrain fit with a Log-Normal Probability Distribution Function (PDF) ($R^2 = 0.99$). Also plotted is the distribution mean (σ^0_{mean}), the 5th percentile ($\sigma^0_{5\%}$), and the 95th percentile ($\sigma^0_{95\%}$). (b) Raw data points (gray) and σ^0_{mean} in 10° increments from 55° to 95° (red). The error bars for these mean values represent the 5th and 95th percentile values.

crystal sizes ranged between 1 and 5 cm, which translates to a surface roughness of 19.7 and 98.5, respectively, which is well above the threshold of 1.0 set by F. Ulaby et al. (2019) for a surface to be considered very rough. Therefore, a reasonable conclusion from this study is that the roughness of the glacier surface is a dominant factor controlling 94 GHz radar backscatter from glacier ice.

Measurements of σ^0 versus incidence angle of glacier terrain for different radar frequencies are absent from the literature. Instead, we compare our measurements to radar backscatter measurements of multi-year sea ice at X-band, Ku-band, and Ka-band where there is negligible ice penetration (Hensley et al., 2016; Langley et al., 2007, 2009; Rignot et al., 2001; Scott et al., 2006; Wessel et al., 2016) and the surface roughness is similar to alpine glaciers. At X-band, σ^0_{mean} is approximately -13.0 dB for multi-year sea ice but varies between -15.0 and -10.1 dB (Johansson et al., 2017). For snow-covered multi-year sea ice at low incidence angles (0°–50°), σ^0_{mean} was estimated to be -6 dB at Ka-band, varying between -11 and 1 dB, whilst σ^0_{mean} was estimated to be -10.5 dB at Ku-band, varying more widely between -20 dB and -1 dB (Stroeve et al., 2020). Therefore, 94 GHz (W-band) σ^0 from glacier ice is expected to be larger than radars operating at Ku-band and lower frequencies, but may have a similar magnitude to radars operating at Ka-band. Comparison to literature values of σ^0_{mean} for other terrain at 94 GHz (see Supporting Information S1) shows that glacier surfaces (-9.9 dB) are most similar to wet soil (-10.3 dB) and wet snow (-10.6 dB) (Nashashibi et al., 1996; F. Ulaby et al., 2019). Further, we observed widespread melting across the surface of Rhônegletscher during our study which acts to reduce radar backscatter from the glacier surface as water is highly attenuating at 94 GHz. However, the presence of debris on the ice surface causes spatially variable rates of melting and subsequently creates a randomly rough surface that enhances radar backscatter. This effect is known to increase radar backscatter at high incidence angles in wet snow and soil (Nashashibi et al., 1996; F. Ulaby et al., 2019) and explains the gradual increase in glacier ice σ^0 from high (70–90°) to medium (30–70°) incidence angles (Figure 4).

3.3. Evaluating Glacier Processes

We can generate 2D images of the Rhônegletscher surface by extracting the maximum σ^0 at each range bin and azimuth angle as shown in Figure 3d—the aerial image acquired in 2020 from © swisstopo is shown in Figure 3c for context. The σ^0 image in Figure 3d maps the speckle pattern across the scene and results from constructive and destructive interference of glacier surface clutter elements. Surface fractures can be observed when they

are larger than the range resolution (0.75 m) and also follow near-linear paths, whilst icebergs in the proglacial lake can be clearly demarcated due to the high contrast in radar backscatter between water and ice. Locations where $\sigma^0 \geq -10$ dB, such as near the ice terminus, represent regions where the local incidence angle is smaller or the terrain is near to medium incidence angles (55°). Beneath the tarpaulin cover (see Figure 1 for location), surface crevasses have been preserved due to the local reduction in surface melting, but critically 94 GHz radar can penetrate the tarpaulin cover and hence map these linear crevasse features. Values of σ^0 on the eastern side of the glacier (right side of Figure 3d) are lower than the western (left) side which may be attributed to an increase in surface debris in this region given its negative impact on 94 GHz radar backscatter. The calibrated/validated σ^0 maps have great potential for understanding glaciological and cryospheric processes. For example, glacier velocities could be extracted from the 2D speckle patterns using feature-tracking algorithms (Joughin, 2002). Further, changes in σ^0 may provide insights into the conditions of the ice surface such as the diurnal cycle of melt and refreezing, the accumulation and redistribution of snow, and aerodynamic roughness (Chambers et al., 2021; Dachauer et al., 2021; Smith et al., 2016) which impacts glacier surface melt.

4. Conclusions

This study has demonstrated that glacier ice is an effective scattering target at 94 GHz and therefore can be used to accurately map and monitor glaciers at high resolution. To do this, we quantified the distribution of σ^0 at 94 GHz across glacier terrain between 50° and 90° incidence angles. The associated range of σ^0 values were found to be $-17.0 < \sigma^0 < -3.4$; $\sigma^0_{\mathrm{mean}} = -9.9$ dB where the upper and lower bounds were calculated from the 5th $\left(\sigma^0_{5\%}\right)$ and 95th $\left(\sigma^0_{95\%}\right)$ percentile limits, respectively. The distribution closely follows a log-normal distribution and the transition between high and medium incidence angles is not distinct, both of which suggests surface roughness is the primary driver of glacier ice radar backscatter at 94 GHz. Further, the 3D shape of Rhônegletscher was measured using the AVTIS2 94 GHz radar and a comparison to a high-resolution DEM obtained by photogrammetry shows good agreement, with average uncertainties (σ_{A2}) ranging from 1.30 to 3.72 m. Future research should seek to acquire new 94 GHz σ^0 data across a variety of ice surface types, whilst co-located measurements of glacier terrain using multiple radar frequencies would enable direct comparisons of how glacier surface features impact radar backscatter. Algorithms for classifying different terrain types (e.g., snow, ice, debris) could also be developed given the theoretical differences between terrain types.

Data Availability Statement

The Normalised Radar Cross Section $\left(\sigma^0\right)$ data (Figure 4) and the Rhônegletscher point cloud extracted from AVTIS2 data (Figure 3b) are available at the zenodo repository via https://zenodo.org/record/8044935 and are fully open access (Harcourt, Robertson, Macfarlane, Rea, & Spagnolo, 2023). Additional details on data processing and data summaries can be found in Supporting Information S1.

References

Benn, D. I., & Evans, D. J. (2010). *Glaciers & glaciation*. Routledge.

Chambers, J. R., Smith, M. W., Smith, T., Sailer, R., Quincey, D. J., Carrivick, J. L., et al. (2021). Correcting for systematic underestimation of topographic glacier aerodynamic roughness values from Hintereisferner, Austria. *Frontiers in Earth Science*, *9*. https://doi.org/10.3389/feart.2021.691195

Chang, P. S., Mead, J. B., Knapp, E. J., Sadowy, G. A., Davis, R. E., & McIntosh, R. E. (1996). Polarimetric backscatter from fresh and metamorphic snowcover at millimeter wavelengths. *IEEE Transactions on Antennas and Propagation*, *44*(1), 58–73. https://doi.org/10.1109/8.477529

Currie, N., Echard, J., Gary, M., Green, A., Lane, T., & Trostel, J. (1988). Millimeter-wave measurements and analysis of snow-covered ground. *IEEE Transactions on Geoscience and Remote Sensing*, *26*(3), 307–317. https://doi.org/10.1109/36.3033

Currie, N. C., Hayes, R. D., & Trebits, R. N. (1992). *Millimeter-wave radar clutter*. Artech House Radar Library.

Dachauer, A., Hann, R., & Hodson, A. J. (2021). Aerodynamic roughness length of crevassed tidewater glaciers from UAV mapping. *The Cryosphere*, *15*(12), 5513–5528. https://doi.org/10.5194/tc-15-5513-2021

Foessel, A., Chheda, S., & Apostolopoulos, D. (1999). Short-range millimeter-wave radar perception in a polar environment. In *Field and service robotics conference*. Carnegie Mellon University.

Girardeau-Montaut, D., Roux, M., Marc, R., & Thibault, G. (2005). Change detection on points cloud data acquired with a ground laser scanner. In *International archives of photogrammetry, remote sensing and spatial information sciences* (pp. 30–35). ISPRS.

Hambrey, M. J., & Lawson, W. (2000). Structural styles and deformation fields in glaciers: A review. *Geological Society, London, Special Publications*, *176*(1), 59–83. https://doi.org/10.1144/gsl.sp.2000.176.01.06

Harcourt, W. D., Macfarlane, D. G., & Robertson, D. A. (2023). 3D terrain mapping and filtering from coarse resolution data cubes extracted from real-aperture 94 GHz radar. ArXiv e-prints. https://doi.org/10.48550/arXiv.2310.08120

Harcourt, W. D., Robertson, D. A., Macfarlane, D. G., Rea, B. R., & Spagnolo, M. (2023). 94 GHz radar backscatter characteristics of alpine glacier ice [Dataset]. Zenodo. https://doi.org/10.5281/zenodo.8044935

Harcourt, W. D., Robertson, D. A., Macfarlane, D. G., Rea, B. R., Spagnolo, M., Benn, D. I., & James, M. R. (2023). Glacier monitoring using real-aperture 94 GHz radar. *Annals of Glaciology*, *63*(87–89), 116–120. https://doi.org/10.1017/aog.2023.30

Hensley, S., Moller, D., Oveisgharan, S., Michel, T., & Wu, X. (2016). Ka-band mapping and measurements of interferometric penetration of the Greenland ice sheets by the Glistin radar. *Ieee Journal of Selected Topics in Applied Earth Observations and Remote Sensing*, *9*(6), 2436–2450. https://doi.org/10.1109/jstars.2016.2560626

Hudleston, P. J. (2015). Structures and fabrics in glacial ice: A review. *Journal of Structural Geology*, *81*, 1–27. https://doi.org/10.1016/j.jsg.2015.09.003

Huss, M., Schwyn, U., Bauder, A., & Farinotti, D. (2021). *Quantifying the overall effect of artificial glacier melt reduction in Switzerland, 2005–2019* (p. 184). Cold Regions Science and Technology.

ITU-R. (2013). *Recommendation ITU-R p.676-10: Attenuation by atmospheric gases (Tech. Rep.)*. International Telecommunications Union.

James, M. R., Robson, S., & Smith, M. W. (2017). 3-d uncertainty-based topographic change detection with structure-from-motion photogrammetry: Precision maps for ground control and directly georeferenced surveys. *Earth Surface Processes and Landforms*, *42*(12), 1769–1788. https://doi.org/10.1002/esp.4125

Jennings, S. J., & Hambrey, M. J. (2021). Structures and deformation in glaciers and ice sheets. *Reviews of Geophysics*, *59*(3), e2021RG000743. https://doi.org/10.1029/2021rg000743

Johansson, A., King, J., Doulgeris, A. P., Gerland, S., Singha, S., Spreen, G., & Busche, T. (2017). Combined observations of Arctic sea ice with near-coincident colocated X-band, C-band, and L-band SAR satellite remote sensing and helicopter-borne measurements. *Journal of Geophysical Research: Oceans*, *122*(1), 669–691. https://doi.org/10.1002/2016jc012273

Joughin, I. (2002). Ice-sheet velocity mapping: A combined interferometric and speckle-tracking approach. *Annals of Glaciology*, *34*, 195–201. https://doi.org/10.3189/172756402781817978

Kuga, Y., Ulaby, F. T., Haddock, T. F., & DeRoo, R. D. (1991). Millimeter-wave radar scattering from snow 1. Radiative transfer model. *Radio Science*, *26*(2), 329–341. https://doi.org/10.1029/90rs02560

Lague, D., Brodu, N., & Leroux, J. (2013). Accurate 3D comparison of complex topography with terrestrial laser scanner: Application to the Rangitikei Canyon (NZ). *ISPRS Journal of Photogrammetry and Remote Sensing*, *82*, 10–26. https://doi.org/10.1016/j.isprsjprs.2013.04.009

Langley, K., Hamran, S.-E., Hogda, K. A., Storvold, R., Brandt, O., Hagen, J. O., & Kohler, J. (2007). Use of c-band ground penetrating radar to determine backscatter sources within glaciers. *IEEE Transactions on Geoscience and Remote Sensing*, *45*(5), 1236–1246. https://doi.org/10.1109/tgrs.2007.892600

Langley, K., Lacroix, P., Hamran, S.-E., & Brandt, O. (2009). Sources of backscatter at 5.3 GHz from a superimposed ice and firn area revealed by multi-frequency GPR and cores. *Journal of Glaciology*, *55*(190), 373–383. https://doi.org/10.3189/002214309788608660

Macfarlane, D. G., Odbert, H. M., Robertson, D. A., James, M. R., Pinkerton, H., & Wadge, G. (2013). Topographic and thermal mapping of volcanic terrain using the AVTIS ground-based 94-GHz dual-mode radar/radiometric imager. *IEEE Transactions on Geoscience and Remote Sensing*, *51*(1), 455–472. https://doi.org/10.1109/tgrs.2012.2202667

Nashashibi, A., Ulaby, F. T., & Sarabandi, K. (1996). Measurement and modeling of the millimeter-wave backscatter response of soil surfaces. *IEEE Transactions on Geoscience and Remote Sensing*, *34*(2), 561–572. https://doi.org/10.1109/36.485132

Nathanson, F. E., Reilly, J. P., & Cohen, M. N. (1999). *Millimeter-wave radar clutter*. SciTech Publishing.

Noferini, L., Mecatti, D., Macaluso, G., Pieraccini, M., & Atzeni, C. (2009). Monitoring of belvedere glacier using a wide angle GB-SAR interferometer. *Journal of Applied Geophysics*, *68*(2), 289–293. https://doi.org/10.1016/j.jappgeo.2009.02.004

Paul, F., Azzoni, R., Fugazza, D., Le Bris, R., Nemec, J., Rabatel, A., et al. (2015). *Glims glacier database, version 1 (Tech. Rep.)*. GLIMS Consortium.

Rees, W. (1992). Measurement of the fractal dimension of ice-sheet surfaces using Landsat data. *International Journal of Remote Sensing*, *13*(4), 663–671. https://doi.org/10.1080/01431169208904144

Rignot, E., Echelmeyer, K., & Krabill, W. (2001). Penetration depth of interferometric synthetic-aperture radar signals in snow and ice. *Geophysical Research Letters*, *28*(18), 3501–3504. https://doi.org/10.1029/2000gl012484

Scott, J. B., Mair, D., Nienow, P., Parry, V., & Morris, E. (2006). A ground-based radar backscatter investigation in the percolation zone of the Greenland ice sheet. *Remote Sensing of Environment*, *104*(4), 361–373. https://doi.org/10.1016/j.rse.2006.05.009

Smith, M. W., Quincey, D. J., Dixon, T., Bingham, R. G., Carrivick, J. L., Irvine-Fynn, T. D., & Rippin, D. M. (2016). Aerodynamic roughness of glacial ice surfaces derived from high-resolution topographic data. *Journal of Geophysical Research: Earth Surface*, *121*(4), 748–766. https://doi.org/10.1002/2015jf003759

Stroeve, J., Nandan, V., Willatt, R., Tonboe, R., Hendricks, S., Ricker, R., et al. (2020). Surface-based Ku-and Ka-band polarimetric radar for sea ice studies. *The Cryosphere*, *14*(12), 4405–4426. https://doi.org/10.5194/tc-14-4405-2020

Ulaby, F., Dobson, M. C., & Álvarez-Pérez, J. L. (2019). *Handbook of radar scattering statistics for terrain*. Artech House.

Ulaby, F. T., Nashashibi, A., El-Rouby, A., Li, E. S., De Roo, R. D., Sarabandi, K., et al. (1998). 95-GHz scattering by terrain at near-grazing incidence. *IEEE Transactions on Antennas and Propagation*, *46*(1), 3–13. https://doi.org/10.1109/8.655446

van den Broeke, M. R. (1997). Momentum, heat, and moisture budgets of the katabatic wind layer over a midlatitude glacier in summer. *Journal of Applied Meteorology*, *36*(6), 763–774. https://doi.org/10.1175/1520-0450(1997)036<0763:mhambo>2.0.co;2

Wang, X., Voytenko, D., & Holland, D. M. (2022). Accuracy evaluation of digital elevation models derived from terrestrial radar interferometer over Helheim Glacier, Greenland. *Remote Sensing of Environment*, *268*, 112759. https://doi.org/10.1016/j.rse.2021.112759

Wessel, B., Bertram, A., Gruber, A., Bemm, S., & Dech, S. (2016). A new high-resolution elevation model of Greenland derived from tandem-x. In *Isprs annals of the photogrammetry, remote sensing and spatial information sciences* (pp. 9–16). ISPRS.

Williams, L. D., Gallagher, J. G., Sugden, D. E., & Birnie, R. V. (1988). Surface snow properties effect on millimeter-wave backscatter. *IEEE Transactions on Geoscience and Remote Sensing*, *26*(3), 300–306. https://doi.org/10.1109/36.3032